MIT Open Access Articles

Quantitative Tissue Spectroscopy of Near Infrared Fluorescent Nanosensor Implants

Massachusetts Institute of Technology

Quantitative Tissue Spectroscopy of Near Infrared Fluorescent Nanosensor Implants

Nicole M. Iverson[1,‡], **Gili Bisker**[2,‡], **Edgardo Farias**[1], **Vsevolod Ivanov**[1], **Jiyoung Ahn**[2], **Gerald N. Wogan**[1], and **Michael S. Strano**[2,*]

[1]Department of Biological Engineering, Massachusetts, Institute of Technology, Cambridge, MA 02139

[2]Department of Chemical Engineering, Massachusetts, Institute of Technology, Cambridge, MA 02139

Abstract

Implantable, near infrared (nIR) fluorescent nanosensors are advantageous for *in vivo* monitoring of biological analytes since they can be rendered selective for particular target molecule while utilizing their unique optical properties and the nIR tissue transparency window for information transfer without an internal power source or telemetry. However, basic questions remain regarding the optimal encapsulation platform, geometrical properties, and concentration ranges required for effective signal to noise ratio through biological tissue. In this work, we systematically explore these variables quantitatively to optimize the performance of such optical nanosensors for biomedical applications. We investigate both alginate and polyethylene glycol (PEG) as model hydrogel systems, encapsulating $d(GT)_{15}$ ssDNA-wrapped single walled carbon nanotubes (SWNT) as model fluorescent nanoparticle sensors, responsive to riboflavin. Hydrogel sensors implanted 0.5 mm into thick tissue samples cause 50% reduction of initial fluorescence intensity, allowing an optical detection limit of 5.4 mm and 5.1 mm depth in tissue for alginate and PEG gels, respectively, at a SWNT concentration of 10 mg L^{-1}, and 785 nm laser excitation of 80 mW and 30 s exposure. These findings are supported with *in vivo* nIR fluorescent imaging of SWNT hydrogels implanted subcutaneously in mice. For the case of SWNT, we find that the alginate system is preferable in terms of emission intensity, sensor response, rheological properties, and shelf life.

Keywords

Nanoparticles; hydrogel; fluorescence; in vivo biosensor; single-walled carbon nanotube

The near infrared region of the electromagnetic spectrum has advantages for in vivo fluorescence imaging[1], due to minimal auto fluorescence and absorption of blood and tissue[2]. Common nIR fluorescent agents include organic nIR fluorophores, such as Indocyanine green (ICG)[3], semiconductor quantum dots (Qdots)[4–6], and single-walled carbon nanotubes (SWNT)[7]. The ICG dye has been used for real time detection of liver cancer[8] and sentinel lymph node mapping in breast cancer patients[9]. Biofunctionalized CdSe/ZnS Qdots[10] and InAs/InP/ZnSe Qdots[11] were used for tumor targeting and fluorescent imaging in mice. Moreover, nIR fluorescent phosphine coated CdTe/CdSe Qdots intradermally injected into mice and pigs were used to map sentinel lymph nodes[12]. These demonstrations exploited the first nIR window (<950 nm), however, the second nIR window (950–1400 nm) provides lower autofluorescence and lower photon scattering, although water absorption is higher[13,14]. Although the properties of quantum dots can be altered to tune their emission peak to longer wavelengths, limited availability of inorganic precursors and their toxicity is still a constraint[15,16].

Single walled carbon nanotubes have great potential for biomedical applications due to their unique optical properties and their ability to fluoresce in the nIR range of 900–1400 nm[7]. Moreover, they are preferable *in vivo* imaging agents as they can be rendered biocompatible with proper surface wrapping[17], and due to their lack of photobleaching[18–20], as opposed to organic dyes and Qdots[21]. An early demonstration of SWNT imaging within a living organism was in *Drosophila melanogaster*, fed SWNT suspended in bovine serum albumin (BSA) solution[22]. Additionally, polyethylene glycol (PEG) coated biocompatible[17] SWNT, localized in the liver and spleen in mice following tail vein injection[14], were fluorescently imaged. The circulation time of SWNT in mice was found to be of the order of 1 day, and total clearance took 2 months, without showing any toxic effects[23]. Recent work demonstrated noninvasive, through skull imaging of the cerebral vasculatures in mice following tail vein injection of PEG-SWNT solution, illustrating the advantages of utilizing the second nIR window for in vivo imaging[24]. Further, bacteriophage functionalized SWNT were utilized for imaging sub-millimeter ovarian tumors[25] and bacterial infections *in vivo*[26].

An additional advantage of SWNT is that tailored functionalization of the nanotube's surface can result in a selective fluorescent modulation upon the interaction with a specific analyte, rendering the SWNT an optical sensor[27–30]. Importantly, *in vivo* localization in a region of interest and the stability of the fluorescent signal once the SWNT are delivered are of crucial importance for any imaging application. One approach to minimize variation in SWNT localization is to encapsulate the nanoparticles within a biocompatible hydrogel that can be implanted within the animal[31].

PEG hydrogels are widely used due to their variability and ease of use, allowing for the equal distribution of functional groups and a large degree of flexibility[32,33]. PEG is also known for its hydrophilicity, biocompatibility, lack of antigenicity and immunogenicity[34], making it an ideal candidate for encapsulation of SWNT sensors. PEG hydrogels are hydrolytically degradable, and their biodegradation kinetics is highly affected by the implantation site and the local tissue environment, exhibiting faster degradation within adipose tissue[35]. Alginate, the most widely used material for microbead formation[36], is a naturally occurring anionic polysaccharide derived from brown algae that also has desirable

properties for SWNT encapsulation. Alginate has been approved for wound dressings and as a cell carrier due to its lack of toxicity[37–39], however it has been found that the ionically bonded hydrogels frequently suffer from degradation, unable to endure the mechanical and chemical strain of implantation and the exchange of cations that occurs under physiological conditions[36,40,41]. Although ionically crosslinked alginate gels can undergo uncontrollable biodegradation while releasing polysaccharide chains from their matrix[42], partial control can be obtained by bimodal molecular weight distribution of the polymer building blocks[43]. In addition, the bio-stability of alginate encapsulating nanoparticles implant was demonstrated in mice for more than 400 days, without any observed degradation or loss of functionality[31].

Essential to the success of a sensor implant is the ability to detect and transmit molecular detection from within the live, intact animal. Recent work showed detection of alginate encapsulated SWNT subcutaneously[31], but other hydrogel delivery platforms, detection limits, and deeper tissue implantation were not investigated. The goal of this work was to provide a quantitative, materials-based framework from which to engineer implantable fluorescent sensors of various kinds. To this end, we analyze the relationship between tissue depth and signal detection for SWNT as a specific example in both alginate and PEG gels and demonstrated *in vivo* fluorescent imaging in mice, facilitating future *in vivo* use of such sensors and determined the potential of these gel encapsulates for deep tissue imaging.

Materials and Methods

DNA Oligonucleotide Nanotube Suspension

SWNT were suspended with a $d(GT)_{15}$ DNA oligonucleotide using methods developed previously[44–46]. Briefly, SWNT purchased from SouthWest NanoTechnologies (SG65i: tube diameter 0.77 ± 0.02 nm; high aspect ratio of $> 1,000$; carbon content $> 95\%$ by weight; $> 40\%$ (6,5) chirality; and $> 95\%$ semiconducting) were suspended with a 30-base $d(GT)_{15}$ sequence of ssDNA (Integrated DNA Technologies). DNA and SWNT were added in a 2:1 DNA:SWNT mass ratio to 0.1 M NaCl dissolved in nanopure water. Typical DNA concentrations used in this study were 2 mg mL^{-1}. The DNA-SWNT solutions on ice were ultrasonicated with a 3 mm probe tip ultrasonicator (Cole Parmer) for 40 min at a power of 3 W, followed by bench top centrifugation for 180 min (Eppendorf Centrifuge 5415D) at 16,100 RCF. The top 80% of the supernatant was collected and the pellet discarded.

Gel Mold

Molds for cross-linking the gels were created by cutting 3.175 mm thick pieces of silicone (HT-6240 transparent 0.125′ performance solid silicone, Rogers Corporation) with a water jet. Shapes chosen for the mold were designed to alter surface area of the gel while keeping the total volume constant.

Alginate-(GT)$_{15}$-SWNT preparation

SWNT were encapsulated within alginate hydrogel as previously described[31]. Briefly, (GT)$_{15}$-SWNT suspension was mixed with 2% PRONOVA SLM 20 alginate (NovaMatrix) dissolved in normal saline and pipetted into molds described above with dialysis tubing (10,000 MWCO) stretched across the bottom and elevated 2 mm from the bottom of a basin.

The alginate was cross-linked for 24 hours with an excess of 0.1 M barium chloride ($BaCl_2$) that was added to the basin without covering the top of the mold. A calcium chloride solution could also be used to cross-link the alginate, but previous studies have shown that similar characteristics and stability result from both cross-linking agents[47] so only $BaCl_2$ was used for these studies. Samples were then transferred to a 0.1 M $BaCl_2$ bath until testing.

PEG-(GT)$_{15}$-SWNT preparation

(GT)$_{15}$-SWNT suspension was mixed with a solution of polyethylene glycol–diacrylate (700 g/mol, Sigma-Aldrich, 1.12 g mL^{-1} at 25 °C), 2-hydroxy-4′-(2-hydroxyethoxy)-2-methylpropiophenone (7 mg mL^{-1}, Sigma-Aldrich) and water in a 1:0.05:0.95 volume ratio[48,49] and pipetted into a mold (described above), with tape adhered to the bottom. The PEG was cross-linked by exposure to UV-B light (365 nm) for 15 minutes and transferred to a water bath until testing.

Optical characterization of SWNT gels

Alginate-(GT)$_{15}$-SWNT and PEG-(GT)$_{15}$-SWNT solutions were prepared as described above. Aliquots (150 μl) of the alginate solution were cast into 2 kDa molecular weight cutoff slide-A-lyzer mini dialysis units and placed in a 0.1 M barium chloride bath for cross-linking. Similarly, 150 μl aliquots of PEG solution were cast into tuning 4.5 mm in diameter and 9 mm in height for cross-linking by UV-B light. The cross-linked PEG and alginate hydrogel plugs were placed in a 96-well plate containing 150 μl water and 150 μl 0.1 M barium chloride in each well, respectively, and allowed to equilibrate for 24 hours before testing.

Fluorescent emission of the SWNT hydrogels was measured in a custom-built near infrared fluorescence microscope (nIR array). In brief, a Zeiss AxioVision inverted microscope was coupled to a Princeton Instruments InGaAs 1-D array detector through a PI-Acton SP150 spectrograph. SWNT solutions were excited using a 785nm, 150 mW (80 mW on the sample plane) photodiode laser (B&W Tek Inc.) with resultant fluorescence collected by the microscope with X20 objective, and coupled optics.

Rheological characterization of SWNT gels

Alginate-(GT)$_{15}$-SWNT and PEG-(GT)$_{15}$-SWNT solutions were prepared as described above and 1.25 ml aliquots were cast for cross-linking in a 20 mm diameter ring mold, forming a hydrogel disk. Rheological characterization was performed on an AR2000 Rheometer (TA Instruments) with a 20 mm parallel steel plate geometry. An adhesive sand paper was used to ensure proper and constant contact of the top and bottom surfaces of the gel. Initial strain sweep was done at 1 Hz frequency, followed by a frequency sweep with 0.1% and 0.01% strain for the alginate and PEG gels respectively.

Tissue Imaging

In vivo imaging was performed on a whole-animal imaging platform described previously[31] using a liquid crystal tunable band-pass filter and a CCD camera (Maestro™ CRi). Filter wavelengths utilized ranged from 650 to 1050 nm at a 40 nm band-pass. Spectral 2D image-

wavelength stacks were background subtracted from any autofluorescence segregated into three components as described previously[31]. Specific images were collected with an emission window from 950 to 1050 nm at 10 nm increments and 20 second integration times at each step.

SWNT fluorescence quenching

SWNT nIR fluorescence spectra for PEG-$(GT)_{15}$-SWNT and alginate-$(GT)_{15}$-SWNT were measured in a 96-well plate on the nIR microscope as described previously[31]. The $(GT)_{15}$-SWNT samples of 150 μL were prepared with concentrations of 2, 5, 10, and 25 mg L^{-1} and tested within a 96-well plate as well. Model quenching experiments were conducted by adding 1.5 μl of 10 mM riboflavin (Sigma) to each well, comparing to control samples to which 1.5 μl of water was added. The samples were incubated for 1 hour in room temperature on a shaker and then Imaged in the nIR array.

Photobleaching of SWNT gels

PEG-$(GT)_{15}$-SWNT and alginate-$(GT)_{15}$-SWNT were placed on moistened filter paper (BioRad mini Trans-Blot), exposed to a 651 nm 14 mW laser and imaged by the animal imaging system every 5 minutes for a 4 hour interval. Samples were continuously exposed to laser irradiation for the entire course of the photobleaching study.

Long term stability of SWNT gels

PEG-$(GT)_{15}$-SWNT and alginate-$(GT)_{15}$-SWNT were periodically analyzed over 60 days on the nIR array and whole animal imaging systems. Gels were imaged as described above and stored in their buffer solutions (water and $BaCl_2$ for PEG and alginate gels respectively) at 25°C between imaging.

Tissue depth detection with phantom tissue

Chicken breast was selected as a phantom tissue for use in these experiments. Chicken breast samples were kept frozen and were thawed at room temperature shortly before testing. Tissue sections with a uniform radius of 2 cm were prepared at thicknesses of 2, 4, 6, 8 or 10 mm. A 1 cm thick section of tissue with a gel sample located in the center was placed on the whole animal imaging platform, and an experimental tissue of specified thickness was placed on top of this stack for imaging. This process was repeated with three different gels and three different sample tissues for each thickness tested. For the nIR array imaging system, slices of various thicknesses of chicken breast tissue were placed on a microscope slide, and gel plugs were placed on top of the tissue sample. The exposure times for the PEG hydrogels were 9, 14, 16, 24, and 36 seconds for 0, 1, 2, 3, and 4 mm thick samples respectively, and 4, 6, 8, 12, and 20 seconds for the alginate gels, for the same thickness of chicken breast samples. The absorption of the chicken breast tissue was measured using a UV-Visible-nIR spectrophotometer (UV-3101 PC Shimadzu).

Results and discussion

Hydrogel Characterization

Alginate and PEG hydrogels encapsulating (GT)$_{15}$-SWNT of various concentration were prepared and cross-linked in a barium chloride bath or by UV illumination, respectively (Figure 1a). The fluorescent signals of the (GT)$_{15}$-SWNT, alginate-(GT)$_{15}$-SWNT and PEG-(GT)$_{15}$-SWNT induced by 2 second exposures are shown in Figure 1b. The spectra were deconvoluted to the different SWNT chiralities (see supporting information Figure S3) and the peak values of the fluorescence signal of the (6,5) tubes are summarized in Figure 1c. The fluorescent signal of SWNT increases linearly with increasing concentration for low concentrations[50], reaching a plateau above 10 mg L^{-1} (dotted lines in Figure 1c), whereas the PEG-(GT)$_{15}$-SWNT and alginate-(GT)$_{15}$-SWNT hydrogels, at 25 mg L^{-1} show a decrease in fluorescence emission, therefore creating an optimal SWNT nanoparticle concentration at 10 mg L^{-1} for both hydrogels. At all concentrations tested, the alginate gels show 1–3 times greater fluorescence than PEG hydrogels. Moreover, the (6,5) peak fluorescence of the alginate and PEG gels is red shifted (by 2–6 nm) compared to the SWNT (Figure 1d), indicating an increase in the dielectric constant of the surrounding medium[51]. The red shift also indicates a partial removal of the DNA wrapping, exposing the SWNT surface to additional water molecules[52–54], and possible SWNT aggregation within the gel[55], which contributes to decreased fluorescence emission at high concentration. This effect must be taken under consideration in any system of hydrogel encapsulation, since increasing nanoparticle concentration can lead to self-quenching for metallic nanotube containing mixtures[56]. This solvatochromic shift, resulting from the polarizability of the SWNT exciton, was shown to have the functional form[52–54]:

$$(E_{ii})^2 \Delta E_{ii} = -Lk \left[\frac{2(\varepsilon-1)}{2\varepsilon+1} - \frac{2(\varepsilon_\infty-1)}{2\varepsilon_\infty+1} \right] \frac{1}{R^4} = \frac{c}{R^4} \quad (1)$$

where E_{ii} are the optical transition energies of pristine SWNT in air, E_{ii} is the difference in emission energies between pristine SWNT in air and SWNT in a dielectric environment, L is a fluctuation factor, k is a constant, ε is the static dielectric constant, ε_∞ is the dielectric constant of infinite (optical) frequencies, and R is the nanotube radius. The solvatochromic shifts of (GT)$_{15}$-SWNT, alginate-(GT)$_{15}$-SWNT, and PEG-(GT)$_{15}$-SWNT are plotted in Figure 1e versus d^{-4}, where d is the tube diameter. Optical transition energies of the various chiralities in the sample were calculated based on spectra deconvolution, and the E_{11} optical transition energies of SWNT in air were calculated according to[52]:

$$E_{11}^{air} = \frac{hc}{A_1+A_d d} + A_3 \frac{\cos\theta}{d^2} \quad (2)$$

where h is planck's constant, c is the speed of light, $A_1 = 61.1$ nm, $A_2 = 1113.6$, θ is the chiral angel of an (n,m) nanotube, and $A_3 = -0.077$ eV·nm^2 for mod$((n-m),3)=1$, or $A_3 = 0.032$ eV·nm^2 for mod$((n-m),3)=2$.

The corresponding slopes of the linear fits are 0.0641 eV^{3}nm^4, 0.0696 eV^{3}nm^4, and 0.0718 eV^{3}nm^4, for (GT)$_{15}$-SWNT, alginate-(GT)$_{15}$-SWNT, and PEG-(GT)$_{15}$-SWNT, respectively, and they can be used to estimate the effective dielectric constant at the surface of the nanotubes by comparing them to a reference system:

$$\frac{c}{c_{ref}} = \frac{\frac{2(\varepsilon-1)}{2\varepsilon+1} - \frac{2(\varepsilon_\infty-1)}{2\varepsilon_\infty+1}}{\frac{2(\varepsilon_{ref}-1)}{2\varepsilon_{ref}+1} - \frac{2(\varepsilon_{ref,\infty}-1)}{2\varepsilon_{ref,\infty}+1}} \quad (3)$$

where the subscript *ref* refers to a known reference. We used the results of SWNT suspended in n-methyl-2-pyrrolydone (NMP)[52] where C_{ref}=0.060 eV^{3}nm^4, ε_{ref}=32.2 and $\varepsilon_{\infty,ref}$=1.47, and assumed that ε_∞ for the DNA-wrapped SWNT is equal to that of water ($\varepsilon_{\infty,H_2O}$=1.333). The effective dielectric constant obtained from equation (3) can be attributed to joint contributions from the water and the DNA wrapping, giving an estimation of the relative nanotube surface coverage by the DNA strands:

$$\varepsilon = \alpha \varepsilon_{DNA} + (1-\alpha)\varepsilon_{H_2O} \quad (4)$$

Using the dielectric constants for DNA ε_{DNA}=4[44], and water ε_{H_2O}=80.1[57], we find that the relative surface coverages are 87.2%, 71.9% and 55.3% for (GT)$_{15}$-SWNT in solution, alginate-(GT)$_{15}$-SWNT, and PEG-(GT)$_{15}$-SWNT, respectively, in agreement with the observed red-shift of the emission peaks of SWNT within the hydrogels relative to SWNT emission in solution (Figure 1d). This finding supports the hypothesis of partial displacement of the DNA wrapping upon introduction into the hydrogel and explains the decreased fluorescence emission intensity within the PEG relative to the alginate hydrogels.

Rheological properties of the alginate and PEG gels were determined by oscillatory measurements with parallel plate geometry. The linear viscoelastic region (LVR) of the hydrogels without nanoparticles was assessed by a strain sweep with a constant 1 Hz frequency. The storage (G') and loss (G'') moduli as a function of the strain percentage are presented in Figures 2a and 2b for alginate and PEG respectively. The viscoelastic responses of the gels alone and those containing 2, 5, 10, and 25 mg L^{-1} SWNT were evaluated by a frequency sweep in the LVR, at constant 0.1 % and 0.01 % strain for alginate and PEG respectively (Figures 2c and 2d). The G' values were approximately one order of magnitude larger than the G'' values in all cases. Moreover, the viscoelastic properties showed little variation with respect to nanoparticle concentration, with the exception of the PEG hydrogel with the highest SWNT concentration (25 mg L^{-1}), which had much lower storage modulus compared to lower concentrations. This can possibly be attributed to the high UV absorption of the SWNT which might interfere with the UV-initiated cross-linking. Overall, the alginate hydrogels are less stiff than their PEG counterparts and can sustain higher strain deformations before undergoing mechanical failure. The rigidity of the PEG gels may be a limiting factor for *in vivo* applications since natural tissue movement requires a compliant gel. Reducing PEG concentration or shortening the duration of UV cross-linking may decrease rigidity, and improve the gel properties for *in vivo* applications.

The cross-linking density ρ_x can be estimated from the storage modulus (G') of the hydrogels using the rubber elasticity theory[58–60]:

$$G' = \rho_x RT \quad (5)$$

where R is the gas constant and T is the temperature. Using the G' value in the LVR regions (Figure 2a,b) we found the cross-linking density of alginate and PEG hydrogels to be 48 mol m^{-3} and 363 mol m^{-3}, suggesting an average distance of 3.2 nm and 1.7 nm between cross-links, respectively. Although the theory of rubber elasticity was developed for chemically cross-linked hydrogels[60], such as PEG, equation (5) can be applied to alginate, which is physically cross-linked, under certain conditions such as insignificant dependence of the storage modulus G' on the frequency, and low loss ratio (G'/G'')[61], conditions that apply in this case.

Encapsulated nanoparticles fluorescence quenching in various hydrogel geometries

In order to simulate and characterize an encapsulated nanoparticle sensor, fluorescent modulation of (GT)$_{15}$-SWNT, PEG-(GT)$_{15}$-SWNT and alginate-(GT)$_{15}$-SWNT in response to addition of riboflavin was measured in the nIR array, with results shown in Figure 3a. Riboflavin, whose hydrodynamic radius is 0.58 nm[62], was chosen as a model target analyte since it is a known fluorescence quencher of DNA-wrapped SWNT[29,45]. When exposed to riboflavin at t = 0 min, the fluorescent signal of the SWNT in the alginate gels decreased significantly, where the nanoparticles in the PEG hydrogel showed little to no response. Following 1 hour incubation the signal of the SWNT solutions was quenched by 90%, 85%, 80% and 70% for the 2, 5, 10, and 25 mg L^{-1} concentrations, respectively, while the alginate hydrogels were quenched by 50%, 44%, 48% and 33%, respectively. The PEG hydrogels showed less than 5% change for all concentrations; indeed, incubation for up to 6 hours also showed no significant change (data not shown). Since the average distance between cross-linking points in the alginate gel was almost twice of that in the PEG (3.2 nm and 1.7 nm, respectively), we conclude that signal modulation within the PEG hydrogels is hindered due to internal diffusion limitations.

Properties of both alginate and PEG gels are affected by varying final concentration of the gel solution prior to cross-linking, so composition of the gel must be adapted to desired analyte properties and the detection time scale required. Modulation of the hydrogel pore size can be exploited for increased specificity by excluding molecules with lower diffusion rates, or higher hydrodynamic radius, than the analyte of interest.

We further investigated the effect of nanoparticles concentration by measuring quenching of the alginate hydrogels with 2, 5, 10 and 25 mg L^{-1} SWNT concentrations over a 6 hour period. Two characteristic quenching time scales were found using a bi-exponential fit (Figure 3b), the short being 14.2, 14.5, 14.1, and 15.4 minutes, and the long being 6.18, 5.6, 5.8, and 5.7 hours for the 2, 5, 10, and 25 mg L^{-1} concentrations, respectively. Although initial intensities varied among the four concentrations, the quenching rates were similar for all, suggesting a common mechanism.

The characteristic short and long time scales in the case of the SWNT fluorescent quenching within the alginate hydrogel system are attributed to the riboflavin-SWNT reaction and the riboflavin diffusion, respectively. The riboflavin diffusion coefficient D_R in solution (3.23×10^{-10} m^{2}s^{-1})[63] gives an approximation of an upper bound of the diffusion time of 8 hours for 3 mm gel thickness, in agreement with our experimental results. The shorter diffusion time in alginate, relative to PEG, enables rapid signal modulation by analytes of similar hydrodynamic radius, where the PEG gel encapsulation used in our work impedes signal quenching.

The possible impact of geometrical characteristics of alginate gels on diffusion rate was tested by varying either the total volume of the gel or its surface area while monitoring the fluorescent signal modulation of the alginate-(GT)$_{15}$-SWNT system with a nanoparticle concentration of 10 mg L^{-1} in response to riboflavin. However, the overall dimensions of the hydrogels were kept compatible for *in vivo* testing within a small animal model[31]. The fluorescent signal of circle shaped alginate gels of volumes 200 μl and 600 μl was monitored for 6 hours (Figure 3c). Both the small (200 μL) and large (600 μL) circular gels showed two characteristic quenching times in a bi-exponential fit, one on the order of 20 minutes (20.7 and 26.2 min, respectively), and a second on the order of several hours (6.5 and 10.8 hr, respectively). The comparable time scales demonstrate that minimizing the base surface area of the gel has a minor effect on increasing the quenching rate for a fixed gel height (3 mm), given that it is small relative to the gel diameter (7 mm and 15 mm, respectively). To determine the effect of surface area on quenching we studied star, rectangle, and circle shaped gels, all with identical volume. The long characteristic quenching times in a bi-exponential fit (Figure 3d) were 15.6, 9.9, and 9.5 hours, respectively, showing a slight decrease for smaller lateral surface area. The short characteristic quenching times were comparable for all shapes, being 34.9, 19.3, and 26.8 minutes for the star, rectangle, and circle shaped gels, respectively. Results from these two studies indicate that changing the size and shape of the lateral dimension of the alginate hydrogel, at constant thickness has little effect on the quenching rate. Since the thickness of the gels was small relative to their diameter, diffusion was dominated by the transverse component along the z-axis (Figure 3c and d), therefore internal mass transport is primarily invariant to changes in the size of the gel. In addition, shape, and therefore surface area, of the gel was also found to have only a minor effect on quenching rates, implying that mass transfer at the gel surface is not dependent on the shape of the gel. Larger form factors, however, might suffer from diffusion limitations and would require proper calibration for detection in real time[64].

Chemical stability of the hydrogels

We tested the photothermal and photochemical stability of the two hydrogel model systems by monitoring the fluorescent signal of the encapsulated nanoparticles over time. Since SWNT exhibit no photobleaching[18–20], their fluorescence served as an indicator for degradation of the hydrogel matrix. We imaged the gels for 4 hours under continuous laser excitation of 14 mW at the focal plane, with image collection at 5 minutes intervals. The stability of the signal is clearly evident in Figure 4a for both the alginate and the PEG gels (SWNT at 10 mg L^{-1}) when the samples remained hydrated during testing. However, if the

samples were dried out, they irreversibly lost their shape and fluorescence, which did not recover upon rehydration.

To assess the long-term chemical stability of the nanoparticle encapsulated gels, the fluorescent signal of the SWNT encapsulated within both alginate and PEG hydrogels was monitored for 60 days. Peak fluorescence was measured at multiple time points in the nIR array with SWNT concentration of 2, 5, 10 and 25 mg L^{-1}, and was normalized by the fluorescent peak signal of a standard SWNT suspension measured each time in the same condition of the gels (Figure 4b).

Since alginate hydrogels typically equilibrate within 24 hours[60], the normalized fluorescence of the SWNT encapsulated within the alginate hydrogels was fitted by a biexponential function (Figure 4b) revealing two characteristic time scales, corresponding to an equilibrium process (t_1) of the order of 1 day, and slow degradation (t_2) of the order of 2 years (Figure 4d, blue diamonds and blue squares, respectively), mainly attributed to diffusion of the divalent cations[65,66]. On the other hand, the normalized fluorescence of the SWNT within the PEG hydrogel was fitted by a monoexponential decay function (Figure 4c), owing to a faster equilibrium of the order of 20 minutes[67] which was not captured in this experiment. The degradation time scale (t_2) of the PEG gel system was of the order of 10–100 days (Figure 4e, red circles), primarily caused by hydrolysis[35,68,69].

Furthermore, according to the whole animal imaging system, which integrates the fluorescent signal over the range of 950–1050 nm, the alginate gels better retained their shape along with their fluorescence over the entire test period, whereas the PEG hydrogels lost both their fluorescence and their physical shape (Figure 4e, and supplementary Figure S4).

The two measurement techniques for long term stability experiments manifested significantly longer chemical stability of alginate gels compared to the PEG hydrogels, rendering them more appropriate for long term *in vivo* sensing and detection. Further benefit from this knowledge is that this provides an opportunity for preparation of hydrogels in larger batches, decreasing production time and sample variability. Impaired stability of the PEG hydrogel relative to the alginate can be partly attributed to the significant UV absorption of the nanoparticles used in this study, which can interfere with the photo-induced cross-linking of the PEG hydrogel utilizing this part of the spectrum. Moreover, the chemical stability of the PEG hydrogel poses a limit on the desired range of cross-linking density, since higher density may improve stability, but would reduce diffusion rates of the target analytes through its pores, and hinder SWNT sensor functionality. Since hydrogels encapsulating lower nanoparticle concentrations were shown to exhibit longer shelf life, long term applications will benefit from use of lowest concentration allowing reliable signal detection.

Detection depth limit

In order to estimate the maximal detection depth within tissue, the nanoparticles fluorescent signal was recorded in tissue phantom samples, and the tissue extinction coefficients were estimated by fitting a simple optical fluorescence model and Beer-Lambert law[70]. Assuming

one dimensional absorption and scattering, and a hydrogel of length l encapsulating low concentration of fluorescent nanoparticles, imaged through tissue of thickness d, the detected fluorescence intensity F is[50]:

$$F = A I_0 e^{-(\mu_{ex} + \mu_{em})d} \phi n \sigma l \quad (6)$$

where I_0 is the excitation laser intensity, μ_{ex} and μ_{em} are the tissue extinction coefficients for the excitation and emission wavelengths, respectively, ϕ is the quantum yield, n is the fluorescent nanoparticles number density in the hydrogel, σ is the nanoparticles absorption cross section, and A is a constant taking into account the detector solid angle and efficiency.

$(GT)_{15}$-SWNT encapsulated within PEG and alginate hydrogels were imaged through chicken breast tissue of various thicknesses (Figure 5a) with 785 nm laser excitation, which was chosen in order to benefit from the nIR tissue transparency window. The normalized fluorescent signal measured by the nIR array of the alginate-$(GT)_{15}$-SWNT and the PEG-$(GT)_{15}$-SWNT as a function of the tissue thickness is presented in Figure 5b for the various concentrations used. The fluorescent intensity was evaluated at the (6,5) chirality emission peak normalized by the SWNT concentration and the exposure time such that the data points would collapse to a single curve, assuming linear dependence of the fluorescent signal on the exposure time. Since the fluorescent intensity is linearly dependent on the SWNT concentration only up to 10 mg L^{-1}, only the results for the 2, 5, and 10 mg L^{-1} were fitted by an exponential decay function. The absolute values of the exponent coefficients were 1.325 ± 0.095 mm^{-1} and 1.257 ± 0.103 mm^{-1} for the alginate and PEG gels respectively.

To determine maximal detection depth, we defined a detection limit to be three times the root mean square of the background noise signal of the nIR array imaging system, and maximal exposure time of 30 seconds. The calculation was based on the exponential fit function for the 2, 5, and 10 mg L^{-1} SWNT concentrations. The detection limits are summarized in Table 1.

According to the 1D model presented in equation (6), the exponential coefficient is equal to the sum of the extinction coefficients of the excitation and emission wavelengths, which were evaluated independently by measurement of the absorption spectrum of chicken breast tissue (supplementary Figure S1b) in the corresponding spectral range. The sum of the extinction coefficients corresponding to the excitation laser wavelength (785 nm) and the emitted fluorescence wavelength (996 nm) was 2.121 ± 0.022 mm^{-1} according to the spectrum, which is comparable to the coefficients found in the exponential fit.

Maximum detection limit was further analyzed by imaging with the whole animal imaging system at depths of 2, 4, 6 and 8 mm. This data (Figure 5c) confirmed the nIR results, showing a clear signal for 10 mg L^{-1} gels at 2 and 4 mm depths, whereas the readings of 6 and 8 mm deep samples where comparable to the background noise of the instrument.

The data from two imaging instruments showed that $(GT)_{15}$-SWNT encapsulated in PEG and alginate hydrogels can be imaged within tissue in the nIR array and in the whole animal imaging systems for more than 4 mm in depth, depending on the exposure time and the

excitation intensity, where the signal is reduced to half of its maximal value after approximately 0.55 mm and 0.52 nm for PEG and alginate, respectively. Therefore subcutaneous or intraperitoneal implants of such constructs can be optically imaged by an external device in a noninvasive manner, enabling real time *in vivo* detection and sensing of analytes. For experimental animal research purposes such a platform could potentially reduce the number of animals required by external monitoring of biomarkers of interest. It should be noted, however, that different tissue types are likely to have depth limits for fluorescence detection that are different than those for skeletal muscle, which was the object of this study.

The maximal detection depth for our specific setup and instrumentation, which was found to be of the order of magnitude of 4 – 5 mm, need not be a limiting factor for deeper tissue detection, even for large animals or humans, since possible optimization of the experimental parameters could extend the working range. By extending the exposure time, or increasing the excitation laser intensity above 14 mW or 80 mW, in the whole animal imaging system or in the nIR array, respectively, the enhanced emission signal could penetrate thicker tissue. In this case, the limitation would be the biosafety restrictions that are specific for laser wavelength and tissue pigmentation. Moreover, improving the signal collection efficiency would increase the signal to noise ratio, allowing for deeper tissue imaging. Alternately, the detection depth limit could be overcome with a minimally invasive procedure of surgically inserting an endoscopic optical fiber[71] to the implementation region to transfer the excitation and detection light channels. However, the 1D approximation in the model employed above limits the results to an overestimation of the detection depth.

In vivo detection

In order to evaluate properties of the gels *in vivo*, we implanted PEG and alginate gels encapsulating the fluorescent nanoparticles in mice (n=3) and recorded the fluorescent signal in the whole animal imaging system. As seen in Figure 5d, both PEG and alginate gels were visible 14 days post implantation confirming the feasibility of this hydrogel-sensor system for *in vivo* sensing and detection of analytes. Mice retained implants for 60 days and showed no adverse reactions to either hydrogel.

Conclusions

We have quantitatively explored variables related to hydrogel mechanical and optical properties to optimize the performance of implantable hydrogel-encapsulating sensors for biomedical applications and determined the extent to which these gels can be utilized *in vivo*. We have developed a consistent and reproducible method for hydrogel fabrication of various geometries, including both alginate and polyethylene glycol (PEG) as models of the hydrogel system and encapsulating $d(GT)_{15}$ ssDNA-wrapped single walled carbon nanotubes as model fluorophore sensors contained therein. We found that implanted hydrogel sensors in tissue phantoms reduce to half of initial intensity at 0.5 mm into thick tissue samples, allowing an optical detection limit of 5.4 mm and 5.1 mm depth in tissue for alginate and PEG gels, respectively, at a SWNT concentration of 10 mg L^{-1}, with 785 nm laser excitation of 80 mW, and 30 s exposure. These findings are supported with *in vivo* nIR

fluorescent imaging of SWNT hydrogels implanted subcutaneously in mice. We find that the alginate system is preferable in terms of emission intensity, signal response, rheological properties, and shelf life, making it a promising platform for *in vivo* detection applications.

Our model, which was demonstrated with the $(GT)_{15}$-DNA wrapped single walled carbon nanotubes, can be applied to other polymers that suspend SWNT and alter the sensor specificity as well as to any other fluorescent nanoparticles. Moreover, the thorough characterization performed in our experiments provide valuable background information for future engineering of such hydrogel-encapsulated nIR fluorescent sensors, assessing their performance and predicting detection depth limit.

Supplementary Material

Refer to Web version on PubMed Central for supplementary material.

Acknowledgments

References

1. Frangioni JV. In vivo near-infrared fluorescence imaging. Current opinion in chemical biology. 2003; 7:626–634. [PubMed: 14580568]

2. Wray S, Cope M, Delpy D, Wyatt J, Reynolds E. Characterization of the near infrared absorption spectra of cytochrome aa3 and haemoglobin for the non-invasive monitoring of cerebral oxygenation. Biochimica et Biophysica Acta. 1988; 933:184–192. [PubMed: 2831976]

3. Schaafsma BE, et al. The clinical use of indocyanine green as a near-infrared fluorescent contrast agent for image-guided oncologic surgery. Journal of Surgical Oncology. 2011; 104:323–332. DOI: 10.1002/jso.21943 [PubMed: 21495033]

4. Michalet X, et al. Quantum dots for live cells, in vivo imaging, and diagnostics. Science. 2005; 307:538–544. DOI: 10.1126/science.1104274 [PubMed: 15681376]

5. Medintz IL, Uyeda HT, Goldman ER, Mattoussi H. Quantum dot bioconjugates for imaging, labelling and sensing. Nature materials. 2005; 4:435–446. DOI: 10.1038/nmat1390 [PubMed: 15928695]

6. Pinaud F, et al. Advances in fluorescence imaging with quantum dot bio-probes. Biomaterials. 2006; 27:1679–1687. DOI: 10.1016/j.biomaterials.2005.11.018 [PubMed: 16318871]

7. Bachilo SM, et al. Structure-Assigned Optical Spectra of Single-Walled Carbon Nanotubes. Science. 2002; 298:2361–2366. DOI: 10.1126/science.1078727 [PubMed: 12459549]

8. Ishizawa T, et al. Real-time identification of liver cancers by using indocyanine green fluorescent imaging. Cancer. 2009; 115:2491–2504. DOI: 10.1002/cncr.24291 [PubMed: 19326450]

9. Troyan SL, et al. The FLARE intraoperative near-infrared fluorescence imaging system: a first-in-human clinical trial in breast cancer sentinel lymph node mapping. Annals of surgical oncology. 2009; 16:2943–2952. DOI: 10.1245/s10434-009-0594-2 [PubMed: 19582506]

10. Gao X, Cui Y, Levenson RM, Chung LW, Nie S. In vivo cancer targeting and imaging with semiconductor quantum dots. Nature biotechnology. 2004; 22:969–976. DOI: 10.1038/nbt994

11. Gao J, et al. In Vivo Tumor-Targeted Fluorescence Imaging Using Near-Infrared Non-Cadmium Quantum Dots. Bioconjugate Chemistry. 2010; 21:604–609. DOI: 10.1021/bc900323v [PubMed: 20369817]

12. Kim S, et al. Near-infrared fluorescent type II quantum dots for sentinel lymph node mapping. Nature biotechnology. 2004; 22:93–97. DOI: 10.1038/nbt920

13. Yi H, et al. M13 Phage-Functionalized Single-Walled Carbon Nanotubes As Nanoprobes for Second Near-Infrared Window Fluorescence Imaging of Targeted Tumors. Nano letters. 2012; 12:1176–1183. DOI: 10.1021/nl2031663 [PubMed: 22268625]

14. Welsher K, et al. A route to brightly fluorescent carbon nanotubes for near-infrared imaging in mice. Nature Nanotechnology. 2009; 4:773–780.

15. Ma Q, Su X. Near-infrared quantum dots: synthesis, functionalization and analytical applications. The Analyst. 2010; 135:1867–1877. DOI: 10.1039/c0an00233j [PubMed: 20563343]

16. Rogach AL, Eychmüller A, Hickey SG, Kershaw SV. Infrared-Emitting Colloidal Nanocrystals: Synthesis, Assembly, Spectroscopy, and Applications. Small. 2007; 3:536–557. DOI: 10.1002/smll.200600625 [PubMed: 17340666]

17. Schipper ML, et al. A pilot toxicology study of single-walled carbon nanotubes in a small sample of mice. Nature Nanotechnology. 2008; 3:216–221.

18. Liu Z, Tabakman S, Welsher K, Dai H. Carbon nanotubes in biology and medicine: In vitro and in vivo detection, imaging and drug delivery. Nano Research. 2009; 2:85–120. [PubMed: 20174481]

19. Cherukuri P, Bachilo SM, Litovsky SH, Weisman RB. Near-infrared fluorescence microscopy of single-walled carbon nanotubes in phagocytic cells. Journal of the American Chemical Society. 2004; 126:15638–15639. [PubMed: 15571374]

20. Graff RA, et al. Achieving individual-nanotube dispersion at high loading in single-walled carbon nanotube composites. Advanced Materials. 2005; 17:980–984.

21. Barone PW, Parker RS, Strano MS. In vivo fluorescence detection of glucose using a single-walled carbon nanotube optical sensor: Design, fluorophore properties, advantages, and disadvantages. Analytical Chemistry. 2005; 77:7556–7562. [PubMed: 16316162]

22. Leeuw TK, et al. Single-walled carbon nanotubes in the intact organism: near-IR imaging and biocompatibility studies in Drosophila. Nano letters. 2007; 7:2650–2654. DOI: 10.1021/nl0710452 [PubMed: 17696559]

23. Liu Z, et al. Circulation and long-term fate of functionalized, biocompatible single-walled carbon nanotubes in mice probed by Raman spectroscopy. Proceedings of the National Academy of Sciences. 2008; 105:1410.

24. Hong G, et al. Through-skull fluorescence imaging of the brain in a new near-infrared window. Nat Photon. 2014; 8:723–730. http://www.nature.com/nphoton/journal/v8/n9/abs/nphoton.2014.166.html - supplementary-information. DOI: 10.1038/nphoton.2014.166

25. Ghosh D, et al. Deep, noninvasive imaging and surgical guidance of submillimeter tumors using targeted M13-stabilized single-walled carbon nanotubes. Proceedings of the National Academy of Sciences. 2014; 111:13948–13953. DOI: 10.1073/pnas.1400821111

26. Bardhan NM, Ghosh D, Belcher AM. Carbon nanotubes as in vivo bacterial probes. Nat Commun. 2014; 5

27. Barone PW, Baik S, Heller DA, Strano MS. Near-infrared optical sensors based on single-walled carbon nanotubes. Nature Materials. 2005; 4:86–U16. [PubMed: 15592477]

28. Kruss S, et al. Carbon nanotubes as optical biomedical sensors. Advanced Drug Delivery Reviews. 2013; 65:1933–1950. doi:http://dx.doi.org/10.1016/j.addr.2013.07.015. [PubMed: 23906934]

29. Zhang J, et al. Molecular recognition using a corona complex made of artificial polymers adsorbed on carbon nanotubes. Nature Nanotechnology. 2013; 8:959–968.

30. Landry M, et al. Experimental Tools to Study Molecular Recognition within the Nanoparticle Corona. Sensors. 2014; 14:16196–16211. [PubMed: 25184487]

31. Iverson NM, et al. In vivo biosensing via tissue-localizable near-infrared-fluorescent single-walled carbon nanotubes. Nat Nano. 2013; 8:873–880. http://www.nature.com/nnano/journal/v8/n11/abs/nnano.2013.222.html - supplementary-information. DOI: 10.1038/nnano.2013.222

32. Arshady R. Beaded polymer supports and gels: II. Physico-chemical criteria and functionalization. Journal of Chromatography A. 1991; 586:199–219.

33. Meldal M. Properties of Solid Supports. Methods in Enzymology. 1997; 289:83–104. [PubMed: 9353719]

34. Wei X, et al. Biodegradable poly(e-caprolactone)–poly(ethylene glycol) copolymers as drug delivery system. International Journal of Pharmaceutics. 2009; 381:1–18. [PubMed: 19664700]

35. Reid B, et al. PEG hydrogel degradation and the role of the surrounding tissue environment. Journal of Tissue Engineering and Regenerative Medicine. 2013 n/a-n/a.

36. Hall KK, Gattás-Asfura KM, Stabler CL. Microencapsulation of islets within alginate/ poly(ethylene glycol) gels cross-linked via Staudinger ligation. Acta Biomaterialia. 2011; 7:614–624. [PubMed: 20654745]

37. Cho WJ, Oh SH, Lee JH. Alginate lm as a novel post-surgical tissue adhesion barrier. Journal of Biomaterials Science Polymer Edition. 2010; 21:701–713. [PubMed: 20482979]

38. Lee KY, Mooney DJ. Alginate: properties and biomedical applications. Progress in Polymer Science. 2012; 37:106–126. [PubMed: 22125349]

39. Ulery BD, Nair LS, Laurencin CT. Biomedical applications of biodegradable polymers. Journal of Polymer Science Part B: Polymer Physics. 2011; 49:832–864.

40. Benson JP, Papas KK, Constantinidis I, Sambanis A. Towards the development of a bioartificial pancreas: effects of poly-L-lysine on alginate beads with BTC3 cells. Cell Transplant. 1997; 6:395–402. [PubMed: 9258513]

41. Thu B, et al. Alginate polycation microcapsules. II. Some functional properties. Biomaterials. 1996; 17:1069–1079. [PubMed: 8718966]

42. Bouhadir KH, et al. Degradation of Partially Oxidized Alginate and Its Potential Application for Tissue Engineering. Biotechnology Progress. 2001; 17:945–950. DOI: 10.1021/bp010070p [PubMed: 11587588]

43. Boontheekul T, Kong H-J, Mooney DJ. Controlling alginate gel degradation utilizing partial oxidation and bimodal molecular weight distribution. Biomaterials. 2005; 26:2455–2465. doi:http://dx.doi.org/10.1016/j.biomaterials.2004.06.044. [PubMed: 15585248]

44. Heller DA, et al. Optical Detection of DNA Conformational Polymorphism on Single-Walled Carbon Nanotubes. Science. 2006; 311:508–511. [PubMed: 16439657]

45. Zhang JQ, et al. Single Molecule Detection of Nitric Oxide Enabled by d(AT)(15) DNA Adsorbed to Near Infrared Fluorescent Single-Walled Carbon Nanotubes. Journal of the American Chemical Society. 2011; 133:567–581. [PubMed: 21142158]

46. Kruss S, et al. Neurotransmitter Detection Using Corona Phase Molecular Recognition on Fluorescent Single-Walled Carbon Nanotube Sensors. Journal of the American Chemical Society. 2013; 136:713–724. DOI: 10.1021/ja410433b

47. Shoichet MS, Li RH, White ML, Winn SR. Stability of Hydrogels Used in Cell Encapsulation - An in-Vitro Comparison of Alginate and Agarose. Biotechnology and Bioengineering. 1996; 50:374–381. [PubMed: 18626986]

48. Kruss S, Erpenbeck L, Schon MP, Spatz JP. Circular, nanostructured and biofunctionalized hydrogel microchannels for dynamic cell adhesion studies. Lab Chip. 2012; 12:3285–3289. DOI: 10.1039/c2lc40611j [PubMed: 22858992]

49. Kruss S, Srot V, van Aken PA, Spatz JP. Au-Ag hybrid nanoparticle patterns of tunable size and density on glass and polymeric supports. Langmuir. 2012; 28:1562–1568. DOI: 10.1021/la204395d [PubMed: 22168477]

50. Fery-Forgues S, Lavabre D. Are Fluorescence Quantum Yields So Tricky to Measure? A Demonstration Using Familiar Stationery Products. Journal of Chemical Education. 1999; 76:1260.

51. Moore VC, et al. Individually Suspended Single-Walled Carbon Nanotubes in Various Surfactants. Nano Lett. 2003; 3:1379–1382. DOI: 10.1021/nl034524j

52. Choi JH, Strano MS. Solvatochromism in single-walled carbon nanotubes. Applied Physics Letters. 2007; 90 223114-223114-223113.

53. Hilmer AJ, Tvrdy K, Zhang J, Strano MS. Charge Transfer Structure–Reactivity Dependence of Fullerene–Single-Walled Carbon Nanotube Heterojunctions. Journal of the American Chemical Society. 2013; 135:11901–11910. DOI: 10.1021/ja404636b [PubMed: 23848070]

54. Mu B, et al. A Structure–Function Relationship for the Optical Modulation of Phenyl Boronic Acid-Grafted, Polyethylene Glycol-Wrapped Single-Walled Carbon Nanotubes. Journal of the American Chemical Society. 2012; 134:17620–17627. DOI: 10.1021/ja307085h [PubMed: 22978786]

55. O'Connell MJ, et al. Band gap fluorescence from individual single-walled carbon nanotubes. Science. 2002; 297:593–596. [PubMed: 12142535]

56. Resch-Genger U, Grabolle M, Cavaliere-Jaricot S, Nitschke R, Nann T. Quantum dots versus organic dyes as fluorescent labels. Nat Meth. 2008; 5:763–775. doi:http://www.nature.com/nmeth/journal/v5/n9/suppinfo/nmeth.1248_S1.html.

57. CRC handbook of chemistry and physics: a ready-reference book of chemical and physical data. Choice: Current Reviews for Academic Libraries. 2010; 47:1251–1251.

58. Wang J, Ugaz VM. Using in situ rheology to characterize the microstructure in photopolymerized polyacrylamide gels for DNA electrophoresis. Electrophoresis. 2006; 27:3349–3358. DOI: 10.1002/elps.200500910 [PubMed: 16892481]

59. Hajighasem A, Kabiri K. Cationic highly alcohol-swellable gels: synthesis and characterization. J Polym Res. 2013; 20:1–9. DOI: 10.1007/s10965-013-0218-1

60. Davidovich-Pinhas M, Bianco-Peled H. A quantitative analysis of alginate swelling. Carbohydrate Polymers. 2010; 79:1020–1027. doi:http://dx.doi.org/10.1016/j.carbpol.2009.10.036.

61. Segeren AJM, Boskamp JV, van den Tempel M. Rheological and swelling properties of alginate gels. Faraday Discussions of the Chemical Society. 1974; 57:255–262. DOI: 10.1039/dc9745700255

62. Tao, X. Smart Fibres, Fabrics and Clothing. Woodhead Publishing; 2001.

63. Sen F, et al. Observation of Oscillatory Surface Reactions of Riboflavin, Trolox, and Singlet Oxygen Using Single Carbon Nanotube Fluorescence Spectroscopy. ACS Nano. 2012; 6:10632–10645. DOI: 10.1021/nn303716n [PubMed: 23075271]

64. Bisker G, Iverson NM, Ahn J, Strano* MS. A Pharmacokinetic Model of a Tissue Implantable Insulin Sensor. Advanced Healthcare Materials. 2014

65. Lee KY, Bouhadir KH, Mooney DJ. Controlled degradation of hydrogels using multi-functional cross-linking molecules. Biomaterials. 2004; 25:2461–2466. doi:http://dx.doi.org/10.1016/j.biomaterials.2003.09.030. [PubMed: 14751730]

66. Kong HJ, Kaigler D, Kim K, Mooney DJ. Controlling Rigidity and Degradation of Alginate Hydrogels via Molecular Weight Distribution. Biomacromolecules. 2004; 5:1720–1727. DOI: 10.1021/bm049879r [PubMed: 15360280]

67. Mellott MB, Searcy K, Pishko MV. Release of protein from highly cross-linked hydrogels of poly(ethylene glycol) diacrylate fabricated by UV polymerization. Biomaterials. 2001; 22:929–941. doi:http://dx.doi.org/10.1016/S0142-9612(00)00258-1. [PubMed: 11311012]

68. Lin C-C, Anseth K. PEG Hydrogels for the Controlled Release of Biomolecules in Regenerative Medicine. Pharm Res. 2009; 26:631–643. DOI: 10.1007/s11095-008-9801-2 [PubMed: 19089601]

69. Metters AT, Bowman CN, Anseth KS. A Statistical Kinetic Model for the Bulk Degradation of PLA-b-PEG-b-PLA Hydrogel Networks. The Journal of Physical Chemistry B. 2000; 104:7043–7049. DOI: 10.1021/jp000523t

70. Robinson, JW. Atomic Spectroscopy, Second Edition. Taylor & Francis; 1996.

71. Yelin D, et al. Three-dimensional miniature endoscopy. Nature. 2006; 443:765–765. doi:http://www.nature.com/nature/journal/v443/n7113/suppinfo/443765a_S1.html. [PubMed: 17051200]
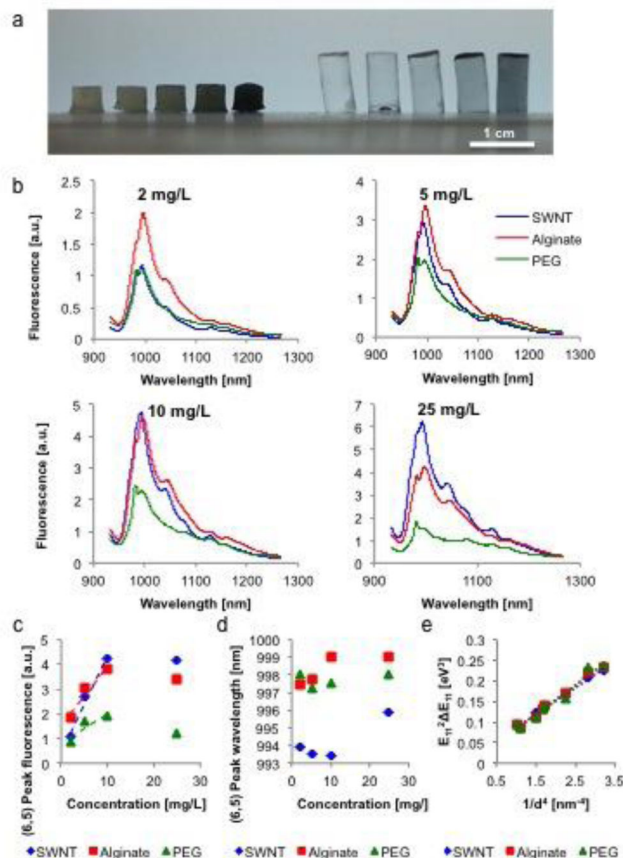
Figure 1.
(a) Image of the alginate (left) and PEG (right) hydrogels with increasing SWNT concentration of 0, 2, 5, 10, and 25 mg L^{-1} (left to right) showing consistent size and shape of gels. (b) Fluorescent emission spectra of $(GT)_{15}$-SWNT solution (blue), alginate-$(GT)_{15}$-SWNT (red), and PEG-$(GT)_{15}$-SWNT (green) for concentrations of 0, 2, 5, 10, and 25 mg L^{-1}. (c) The peak fluorescence of the (6,5) chirality $(GT)_{15}$-SWNT (blue), alginate-$(GT)_{15}$-SWNT (red), and PEG-$(GT)_{15}$-SWNT (green) shows the increase in SWNT fluorescence for the lower concentrations 2, 5 and 10 mg L^{-1}, dotted line is linear fit, but a drop in fluorescence at the higher concentration (25 mg L^{-1}). (d) The wavelength corresponding to the (6,5) chirality peak fluorescence of $(GT)_{15}$-SWNT (blue), alginate-$(GT)_{15}$-SWNT (red), and PEG-$(GT)_{15}$-SWNT (green) shows a red shift for the hydrogels when compared to the non-encapsulated SWNT signal. (e) solvatochromic shift as a function of $1/d^4$ for $(GT)_{15}$-SWNT (blue), alginate-$(GT)_{15}$-SWNT (red), and PEG-$(GT)_{15}$-SWNT (green). Dotted lines are linear fits.
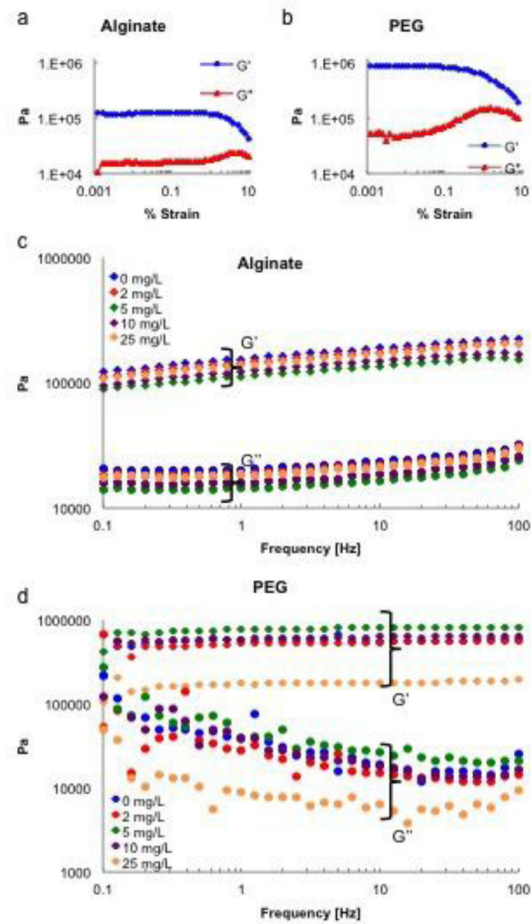
Figure 2.
Rheological properties of the alginate and PEG hydrogels. (a) Strain sweep of alginate and (b) PEG gels with constant 1 Hz frequency. (c) Frequency sweep of alginate gels under 0.1 % strain and of (d) PEG gels under 0.01 % strain.
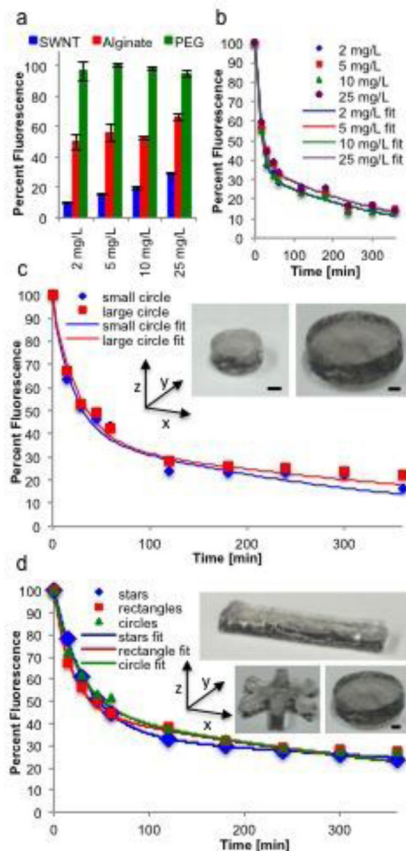
Figure 3.
(a) Fluorescence signal quenching of $(GT)_{15}$-SWNT (blue), alginate-$(GT)_{15}$-SWNT (red), and PEG-$(GT)_{15}$-SWNT (green), measured in the nIR array following 1 hour incubation with riboflavin shows consistent quenching of the SWNT suspension and of alginate encapsulated SWNT, but lack of signal quenching for PEG encapsulated samples. (b–d) Comparison of percent SWNT fluorescence quenching for alginate-$(GT)_{15}$-SWNT during 6 hr of riboflavin exposure, measured on the whole animal imaging system, shows that changing the (b) concentration (c) size and (d) shape/surface area have little effect on quenching rate. Scale bars = 2 mm.
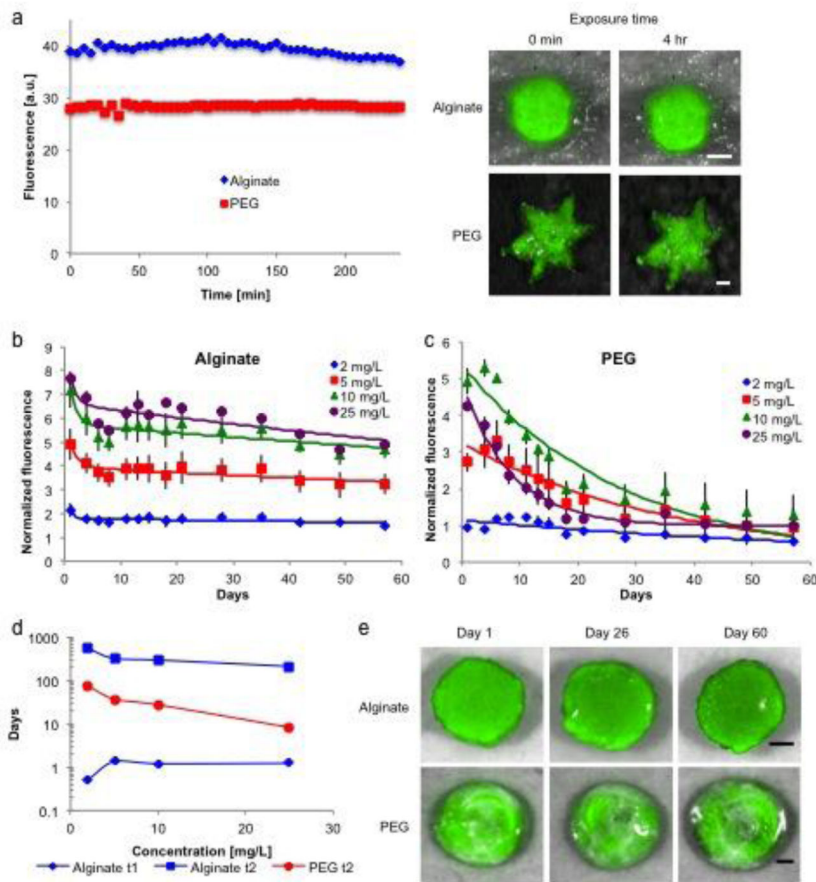
Figure 4.
(a) Short term stability testing of alginate-(GT)$_{15}$-SWNT (blue) and PEG-(GT)$_{15}$-SWNT (red) showed no photobleaching when exposed to laser light for 4 hr. Right: Images of the alginate and PEG hydrogels taken by the whole animal imaging system showing signal stability over 4 hour period. Scale bars = 2 mm. (b) Long term stability of alginate-(GT)$_{15}$-SWNT gels shown by fluorescence signal retention over the 60 day test period. Solid lines represent bi-exponential fit. (c) PEG-(GT)$_{15}$-SWNT gels experience fluorescence signal loss shortly after synthesis. Solid lines represent bi-exponential fit. (d) Shelf life of alginate and PEG gels estimated by the fit function of (b) and (c) corresponds to the observed longevity and breakdown of alginate and PEG hydrogels respectively. (e) Images of alginate-(GT)$_{15}$-SWNT and PEG-(GT)$_{15}$-SWNT acquired on the whole animal imaging system show the gels' retention (alginate) or loss (PEG) of signal over time. Scale bars = 2 mm.
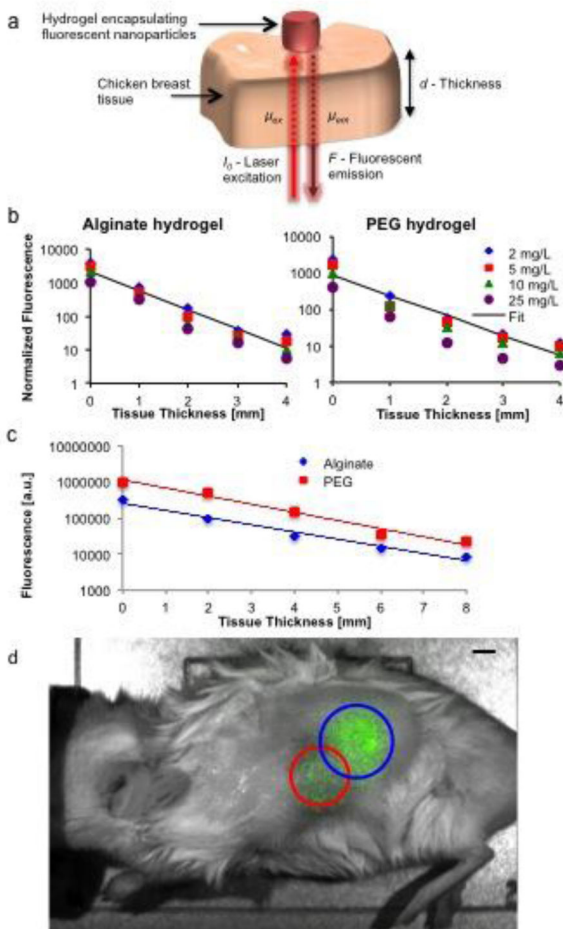
Figure 5.
(a) Illustration of the tissue spectroscopy measurement setup for nIR array analysis. (b) Normalized fluorescent signal of alginate and PEG gels imaged through chicken breast tissue with in house nIR array and (c) whole animal imaging systems. (d) *In vivo* florescent imaging of (GT)$_{15}$-SWNT encapsulated in PEG (red circle) and alginate (blue circle) gels 14 days post implantation; mice showed no negative reactions to the gels and the fluorescence is clearly visible in live animal. Scale bar = 4 mm.

Table 1

Detection limit for the alginate and PEG hydrogel systems determined by the exponential fit function (Equation 6) for the three lower concentration of nanoparticles encapsulated within the hydrogels.

	2 mg L^{-1}	5 mg L^{-1}	10 mg L^{-1}
Alginate	4.1 mm	4.8 mm	5.4 mm
PEG	3.8 mm	4.5 mm	5.1 mm